Reduced phase stability and faster formation/dissociation kinetics in confined methane hydrate

Dongliang Jin, Benoit Coasne

Reduced phase stability and faster formation/dissociation kinetics in confined methane hydrate

Dongliang Jin[a] **and Benoit Coasne**[a,1]

[a]Univ. Grenoble Alpes, CNRS, LIPhy, 38000 Grenoble, France

This manuscript was compiled on September 28, 2021

The mechanisms involved in the formation/dissociation of methane hydrate confined at the nanometer scale are unraveled using advanced molecular modeling techniques combined with a mesoscale thermodynamic approach. By means of atom-scale simulations probing coexistence upon confinement and free energy calculations, phase stability of confined methane hydrate is shown to be restricted to a narrower temperature and pressure domain than its bulk counterpart. The melting point depression at a given pressure, which is consistent with available experimental data, is shown to be quantitatively described using the Gibbs–Thomson formalism if used with accurate estimates for the pore/liquid and pore/hydrate interfacial tensions. The metastability barrier upon hydrate formation and dissociation is found to decrease upon confinement, therefore providing a molecular scale picture for the faster kinetics observed in experiments on confined gas hydrates. By considering different formation mechanisms – bulk homogeneous nucleation, external surface nucleation, and confined nucleation within the porosity – we identify a crossover in the nucleation process; the critical nucleus formed in the pore corresponds either to a hemispherical cap or a bridge nucleus depending on temperature, contact angle, and pore size. Using the classical nucleation theory, for both mechanisms, the typical induction time is shown to scale with the pore volume to surface ratio and, hence, the pore size. These findings for the critical nucleus and nucleation rate associated to such complex transitions provide a mean to rationalize and predict methane hydrate formation in any porous media from simple thermodynamic data.

Gas hydrate | Confinement and porous media | Formation/dissociation kinetics | Thermodynamics and molecular modeling |

Methane hydrate is a non-stoichiometric crystalline phase in which water molecules form hydrogen-bonded cages that entrap methane molecules (1, 2). Under typical terrestrial and marine conditions, methane hydrate forms according to a structure known as sI where 46 water molecules form two small pentagonal dodecahedral cages and six tetracaidecahedral cages so that 8 methane molecules can be encapsulated at most (3). While the large methane hydrate resources available on Earth are still regarded as an important fossil energy source (4), their abundant presence in locations such as seafloor or permafrost is also a threat to the environment as methane is one of the worst greenhouse gases (5, 6). For instance, in the context of increasing concerns about climate change, even weak perturbations such as those induced by a small temperature raise could trigger the dissociation of methane hydrate and release of large amounts of methane into the atmosphere (7). Gas hydrates including methane hydrate are also thought to be a role player in the geochemistry of planets, comets, etc. as typical temperature T and pressure P in many of these systems should promote their formation whenever water and gases are present (8). Finally, methane hydrate is also of particular relevance to energy and environmental science with applications for energy storage and carbon capture (9–13).

The phase diagram of bulk methane hydrate has been the subject of intense research to identify P/T coexistence conditions as well as to determine formation/dissociation mechanisms (14, 15). In contrast, the case of methane hydrate in porous media remains unclear by many aspects with important questions left regarding the role of confinement and surface forces (16–18). Yet, in nature, abundant methane hydrate resources are found in the porosity of rocks and minerals such as in marine sediments, silica sands, permafrost, etc. so that understanding confinement or surface-induced shifts in the phase stability, formation/dissociation kinetics, and composition of gas hydrates is of utmost importance (Fig. 1). Many experimental observations have shown that confinement in pores shifts the liquid–hydrate–vapor (L–H–V) phase boundaries to higher P and/or lower T as a result of capillary forces (19–23). For both organic (e.g. carbonaceous) and mineral (e.g. siliceous) porous environments, such experiments have shown that the shift in melting point qualitatively follows the Gibbs–Thomson equation with ΔT_f scaling linearly with the reciprocal of the pore size D_p, i.e. $\Delta T_f \sim 1/D_p$ [e.g. Refs. (24, 25) and Ref. (20) for a recent review]. This classical macroscopic behavior is found to be reminiscent even at the nanometer

Significance Statement

Large amounts of methane hydrate – which consists of water forming molecular ice cages around methane molecules – are trapped in the porosity of rocks and seafloors. The impact of this so-called "burning ice" on our environment remains unclear (methane is a potent greenhouse gas), especially the parameters driving its phase stability and kinetics. Here, using molecular modeling, we identify the mechanisms involved in the formation/dissociation of confined methane hydrate. The phase stability of confined methane hydrate is shown to be restricted to a narrower temperature/pressure range with faster underlying formation/dissociation kinetics. Such facilitated freezing, which helps rationalize experimental observations, is described using a mesoscale thermodynamic approach of the nucleation mechanism.

Both authors designed the work. D. Jin carried out the molecular simulations while both authors analyzed the data and developed the model. Both authors contributed to the writing of the manuscript.

The authors declare no competing interests.

[1]To whom correspondence should be addressed. E-mail: benoit.coasneuniv-grenoble-alpes.fr

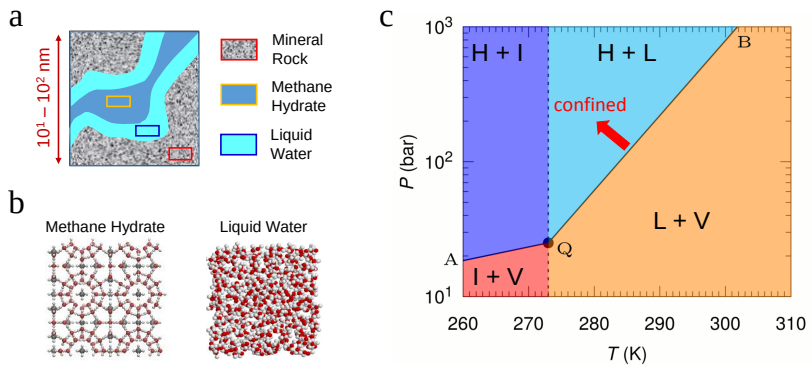

Fig. 1. Phase equilibrium of methane hydrate–liquid water in nanoporous rocks. (a) Illustration of confined liquid water (cyan) and methane hydrate (blue) in a porous rock described with a stone aspect. (b) Typical molecular configurations for methane hydrate (left) and liquid water (right). The red and white spheres are the oxygen and hydrogen atoms of water. The gray spheres are the methane molecules which are located inside the cages formed by water molecules in methane hydrate. (c) Bulk pressure–temperature (P–T) phase diagram for ice (I), liquid (L), hydrate (H), and vapor (V). The dashed line denotes the ice melting line while the solid line A-Q-B corresponds to the hydrate melting line: for a given pressure P, H exists at low T while V exists at high T. Confinement is expected to shift the melting point $P, T_f(P)$ to lower T and larger P.

scale (26) where the validity of bulk macroscopic concepts such as interfacial tension, enthalpy of melting, etc. remains questionable [Fig. 1(b)]. With this respect, while significant efforts are devoted to verifying the scaling law $\Delta T_f \sim 1/D_p$ using molecular simulation for nanoconfined methane hydrate (27), the question of its quantitative validity relying on robust calculations of the pore/liquid and pore/hydrate interfacial tensions and other thermodynamic parameters has not been considered. In fact, while the question of a contact angle θ between solid and liquid phases at a pore surface remains to be addressed, many experimental and theoretical works assume that there is a wetting parameter $\omega = \gamma_{\rm LH} \cos\theta$ that controls the shift in the melting point $\Delta T_f \sim \omega/D_p$ (with the usual assumption $\cos\theta \sim -1$). Beyond confinement-induced shifts in hydrate stability, the formation and dissociation kinetics of these complex compounds remain to be investigated in detail. There are abundant literature data indicating that confinement leads to faster kinetics compared to their bulk counterpart (16, 20, 28) but the underlying microscopic mechanisms remain to be unraveled. Theoretically, much work has been done to elucidate the molecular routes that lead to the nucleation of bulk hydrates (29–33) but the case of confined hydrates has not been considered. Several authors have used molecular modeling to investigate the growth of an already formed methane or carbon dioxide hydrate in the vicinity of a surface (34–38) but microscopic nucleation remains largely unexplored.

Here, we present a theoretical study of confined methane hydrate to elucidate the mechanisms responsible for their reduced phase stability and faster formation/dissociation kinetics. By relying on statistical mechanics, such molecular simulations – using either the direct coexistence method (DCM) or free energy calculations – capture phase coexistence between confined liquid water and methane hydrate. In particular, our approach does not assume any thermodynamic modeling framework or kinetic pathway. We first extend the direct coexistence method to the Grand Canonical ensemble (open ensemble) to account for three phase coexistence (L–H–V) involved in gas hydrate formation/dissociation. Using such atom-scale simulations, we show that the melting point depression for confined hydrate is consistent with the Gibbs–Thomson equation if the pore/liquid and pore/hydrate interfacial tensions are used (here, values were calculated using independent molecular simulations). This macroscopic expression is shown to be a simplified thermodynamic approach that neglects the effect of pressure/temperature and methane chemical potential. In agreement with experimental data, the formation and dissociation of confined methane hydrate as described in our mesoscopic description are faster than for bulk hydrate. By considering different nucleation paths (homogeneous nucleation, surface nucleation, and in-pore nucleation), we identify the critical nucleus leading to the formation of methane hydrate at the surface of the host porous material. This mesoscale thermodynamic approach unravels a crossover in the nucleation process; depending on temperature, the formation of methane hydrate within the porosity involves a critical nucleus that corresponds either to a hemispherical cap or a bridge nucleus. In both cases, within the classical nucleation theory, we derive a single expression for the nucleation rate $1/\tau$ which is found to scale with the material specific surface area or, equivalently, with the reciprocal pore size, $1/\tau \sim 1/D_p$.

Results

Melting point in confinement. Fig. 2(a) illustrates the direct coexistence method (DCM) extended to the Grand Canonical ensemble to investigate the effect of confinement on L–H–V equilibrium (SI *Text*). A hydrate molecular configuration coexisting with liquid water in a slit pore of a size D_p is prepared ($D_p \sim 1.67$ nm, 2.86 nm, 5.23 nm, and 7.61 nm are considered). Using this starting configuration, for a given pressure P, Monte Carlo simulations in the Grand Canonical ensemble (GCMC) are performed for different T to determine the melting temperature T_f as follows. Methane hydrate melts into liquid water for $T > T_f$ [I in Fig. 2(b)] while liquid water crystallizes into methane hydrate for $T < T_f$ [II in Fig. 2(b)]. The Grand Canonical ensemble ensures that L–H–V coexistence is simulated *de facto* (39, 40); because the system is in equilibrium with an infinite reservoir at chemical potentials corresponding to bulk liquid water $\mu_w(P,T)$ and methane vapor $\mu_m(P,T)$ at the same P and T, DCM in this ensemble is equivalent to simulating a three phase coexisting system [$\mu_m(P,T)$ and $\mu_w(P,T)$ are taken from (41)]. It was verified that for $T < T_f$ the methane hydrate occupancy is equivalent to that for bulk methane hydrate by measuring the methane mole fraction in the pore center (through integration of the water/methane density profiles in the region occupied by the methane hydrate except the water/methane layer in contact with the surface). Moreover, the confined hydrate structure was found to correspond to the expected sI structure. As shown in Fig. S1, the order parameter profile $Q_6(z)$ and hydrogen bonds per water molecule $N_{\rm HB}(z)$ measured along the position normal to the surface match those obtained for the sI structure.

Fig. 2(c) shows the methane mole fraction x_m for the slit

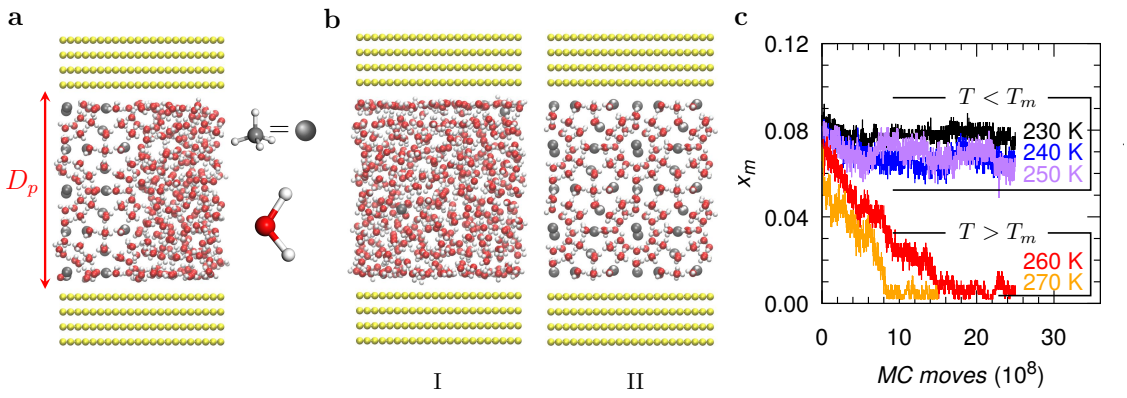

Fig. 2. Probing methane hydrate stability in nanopores. (a) Molecular modeling of phase coexistence in a pore of width $D_p \sim 2.86$ nm. Hydrate and liquid water are located on the left and right, respectively. The red and white spheres are the water oxygen and hydrogen atoms. The gray spheres are methane molecules inside the hydrogen-bonded cages formed by water. The yellow spheres are the solid atoms distributed according to a face-centered square structure. The box dimensions are $L_x = L_y \sim 2.38$ nm. (b) Starting from coexistence in (a), the system evolves towards liquid water or methane hydrate depending on T: (I) for $T > T_f$, hydrate melts, (II) for $T < T_f$, liquid water crystallizes into hydrate (T_f is the melting point of confined hydrate). (c) Change in methane mole fraction x_m during the GCMC simulations at different T.

pore with $D_p \sim 2.86$ nm at different T in the course of GCMC simulations (data for other D_p are given in Figs. S2 and S3); x_m decreases to 0 as the system melts for $T \geq 260$ K while x_m increases upon hydrate formation for $T \leq 250$ K. These data show that $T_f = 255 \pm 5$ K for $D_p \sim 2.86$ nm, which is lower than the bulk melting point taken at the same $P = 100$ atm ($T_{f,0} = 285 \pm 5$ K). This result, which is in qualitative agreement with experimental data on confined methane hydrate, suggests that the pore/hydrate interfacial tension γ_{WH} is larger than the pore/liquid interfacial tension γ_{WL}. The red circles in Fig. 3(c) show the melting point depression $\Delta T_f/T_{f,0}$ obtained using DCM as a function of $1/D_p$ (as shown below, these data are consistent with free energy calculations). In qualitative agreement with the Gibbs–Thomson equation, the scaling $\Delta T_f \sim 1/D_p$ is observed even for such small nanopores. While many experimental and simulation works have validated this scaling, the quantitative verification of the Gibbs–Thomson equation applied to such ultra-confinement has been hampered by limitations in assessing pore/hydrate and pore/liquid interfacial tensions. The effect of surface wettability is assessed here by changing the LJ energy parameter ϵ' of the pore/hydrate and pore/liquid pair interactions. $\epsilon' = \epsilon/2$, $\epsilon/3$, $\epsilon/4$, 2ϵ, 3ϵ, and 4ϵ (where ϵ is the original LJ energy parameter in Table S1) are used to mimic stronger or weaker surface interactions. As shown in Fig. S4, T_f remains constant as ϵ' is varied. This result can be explained using the Gibbs–Thomson equation [Eq. (3)] which will be discussed in detail below. The shift $\Delta T_f/T_{f,0}$ is proportional to the interfacial tension difference $\Delta\gamma = \gamma_{\mathrm{WL}} - \gamma_{\mathrm{WH}}$. At constant T and P, a Taylor expansion for $\Delta\gamma$ leads to $\Delta\gamma(\epsilon') \sim \Delta\gamma(\epsilon) + \partial\Delta\gamma(\epsilon)/\partial\epsilon \times (\epsilon' - \epsilon)$. Surface interactions are found to amount for $< 5\%$ of the energy with negligible impact on $\Delta\gamma$. As a result, $\Delta\gamma(\epsilon') \sim \Delta\gamma(\epsilon)$ so that wettability considered here leads to the same melting shift.

Gibbs–Thomson formalism. Independent molecular simulations were used to determine parameters to assess the quantitative validity of the Gibbs–Thomson equation. Capillary crystallization is described at the macroscopic level using this equation – which is analogous to the Kelvin equation but for liquid/solid transitions. Such thermodynamic model relies on Laplace equation (which links the pressure difference in the confined crystal and liquid to their interfacial tension) combined with the chemical potential equality between the different phases. Two important assumptions are usually made when deriving the Gibbs–Thomson equation: (1) the crystal and liquid have the same molar volume ($v_{\mathrm{C}} \sim v_{\mathrm{L}}$) and (2) Young's equation holds for liquid/solid systems with a contact angle θ ($\gamma_{\mathrm{WL}} - \gamma_{\mathrm{WC}} = \gamma_{\mathrm{LC}} \cos\theta$). While the robustness of the first assumption can be assessed, the second assumption is key as the concept of solid/liquid contact angle in confinement remains unclear. A third assumption, which only pertains to multi-component phases such as hydrates, consists of neglecting the impact of the lowest mole fraction component on stability. For methane hydrate, this assumption consists of deriving phase stability without considering the chemical potential contribution from methane vapor. In what follows, we formally derive the Gibbs–Thomson equation without invoking the contact angle and extends its applicability to binary solids by including the methane contribution into the stability condition. Then, using independent molecular simulations, we estimate the different ingredients to discuss the validity of the Gibbs–Thomson equation when applied to confined hydrate (all derivation steps can be found in SI *Text*).

Let us consider two phases Φ, methane hydrate ($\Phi = \mathrm{H}$) and liquid water with solubilized methane ($\Phi = \mathrm{L}$), in a slit pore of size D_p, surface area A, and pore volume $V = D_p A$ [Fig. 3(a)]. These two phases are in equilibrium with an infinite bulk reservoir which imposes the water and methane chemical potentials μ_w and μ_m, and temperature T. For hydrate/liquid equilibrium in confinement, considering the grand potential $\Omega^\Phi = -P^\Phi V + 2\gamma_{\mathrm{W}\Phi} A$ for each confined phase ($\Phi = \mathrm{L}$, H), the grand potential equality leads to the Laplace equation:

$$P^{\mathrm{L}} - P^{\mathrm{H}} = 2\left(\gamma_{\mathrm{WL}} - \gamma_{\mathrm{WH}}\right)/D_p \qquad [1]$$

where the factor 2 accounts for the two surfaces in the slit geometry. γ_{WH} and γ_{WL} are the pore/hydrate and pore/liquid interfacial tensions at the confined melting point (μ_w, μ_m, T_f). In confinement, as shown in SI *Text*, the pressures P^Φ at the melting point (μ_w, μ_m, T_f) can be expressed using a Taylor

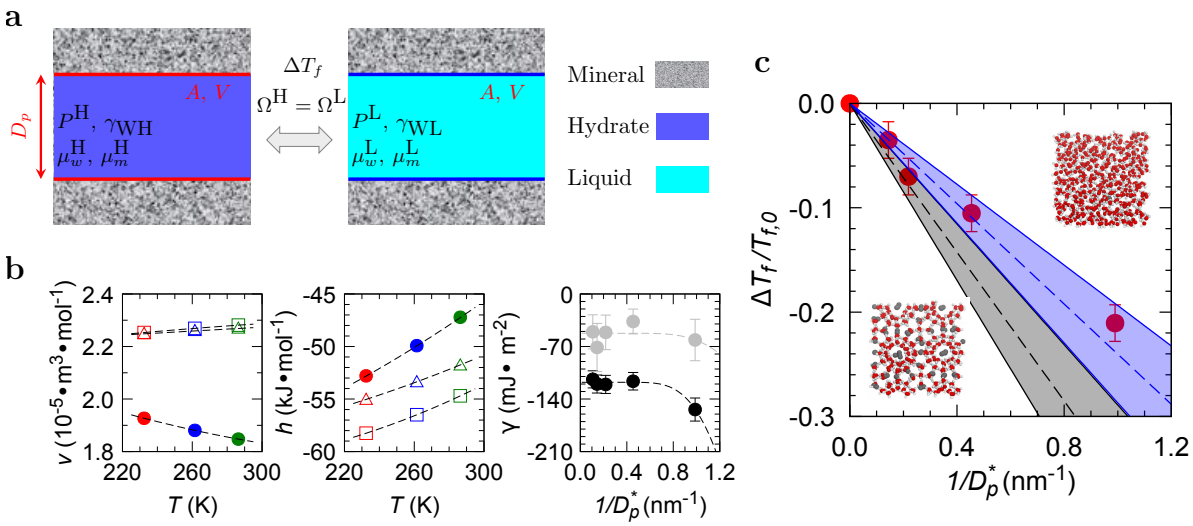

Fig. 3. Gibbs–Thomson effect. (a) L–H–V equilibrium in pores: liquid water (cyan) and hydrate (blue) are confined in a slit pore (gray) of a width D_p, surface area A, and volume V. Ω^{H} and Ω^{L} are the hydrate and water grand potentials at pressures P^{H} and P^{L}. (b) Molar volume v and enthalpy h for liquid water (circles), full-occupancy hydrate (squares), and empty-occupancy hydrate (triangles). These parameters are determined along bulk L–H–V equilibrium at 233 K/1 atm (red), 262 K/10 atm (blue), and 286 K/100 atm (green). The right panel shows the pore/liquid γ_{WL} (black) and pore/hydrate γ_{WH} (gray) interfacial tensions as a function of $1/D_p^*$ [$D_p^* = D_p - 2\sigma^*$ is the pore size accessible to the molecule center of mass]. The dashed lines are fitted against $\gamma(D_p) \sim \gamma^0 + a\exp[-D_p/b]$. (c) Melting shift $\Delta T_f/T_{f,0}$ for confined hydrate T_f with respect to bulk $T_{f,0}$ at $P = 100$ atm as a function of $1/D_p^*$. The solid circles are obtained from the direct coexistence method, while the dashed lines are determined using the Gibbs–Thomson equations: the gray line corresponds to the classical equation [Eq. (4)] while the blue line corresponds to the equation in which the methane chemical potential contribution is accounted for [Eq. (3)]. For each equation, the color shaded area denotes the confidence interval (error bars).

expansion around the bulk melting point ($\mu_{w,0}$, $\mu_{m,0}$, $T_{f,0}$):

$$P^{\mathrm{H}} = P_0 + \frac{1}{v_0^{\mathrm{H}}}\left(\Delta T_f s_0^{\mathrm{H}} + \Delta\mu_w + \Delta\mu_m \frac{x_{m,0}^{\mathrm{H}}}{1-x_{m,0}^{\mathrm{H}}}\right)$$
$$P^{\mathrm{L}} = P_0 + \frac{1}{v_0^{\mathrm{L}}}\left(\Delta T_f s_0^{\mathrm{L}} + \Delta\mu_w + \Delta\mu_m \frac{x_{m,0}^{\mathrm{L}}}{1-x_{m,0}^{\mathrm{L}}}\right) \quad [2]$$

where $P^\Phi = P^\Phi(\mu_w, \mu_m, T_f)$ is the pressure of phase Φ at (μ_w, μ_m, T_f) and $P_0 = P_0^{\mathrm{H}}(\mu_{w,0}, \mu_{m,0}, T_{f,0}) = P_0^{\mathrm{L}}(\mu_{w,0}, \mu_{m,0}, T_{f,0})$ is the pressure at ($\mu_{w,0}$, $\mu_{m,0}$, $T_{f,0}$) [corresponding to $D_p \sim \infty$ in the Laplace equation]. $\Delta T_f = T_f - T_{f,0}$ is the melting temperature shift of confined methane hydrate with respect to its bulk counterpart. $\Delta\mu_i = \Delta\mu_i^\Phi = \mu_i^\Phi - \mu_{i,0}^\Phi$ is the difference of chemical potential μ_i^Φ of species i [i = methane (m), water (w)] for phase Φ at T_f (at this point $\mu_i^{\mathrm{H}} = \mu_i^{\mathrm{L}} = \mu_i$ because of phase coexistence in confinement while also in equilibrium with the external phase) and $T_{f,0}$ (at this point $\mu_{i,0}^{\mathrm{H}} = \mu_{i,0}^{\mathrm{L}} = \mu_{i,0}$ by definition of bulk phase equilibrium). $s_0^\Phi/v_0^\Phi = \partial P/\partial T\,(\mu_{w,0}, \mu_{m,0}, T_{f,0})$ is the molar entropy s_0^Φ (note that s is the total entropy which includes both methane and water contributions) divided by the molar volume v_0^Φ for phase Φ at ($\mu_{w,0}$, $\mu_{m,0}$, $T_{f,0}$). $1/v_0^\Phi = \partial P/\partial\mu_w\,(\mu_{m,0}, \mu_{w,0}, T_{f,0})$ is the reciprocal of the molar volume for phase Φ at ($\mu_{w,0}$, $\mu_{m,0}$, $T_{f,0}$). As established in Eq. (S4), deriving Ω shows that $N_{m,0}^\Phi/N_{w,0}^\Phi v_0^\Phi = \partial P/\partial\mu_m\,(\mu_{m,0}, \mu_{w,0}, T_{f,0})$ is the ratio of the number of methane and water molecules divided by the molar volume v_0^Φ for phases Φ at ($\mu_{w,0}$, $\mu_{m,0}$, $T_{f,0}$). By noting that $N_{m,0}^\Phi/N_{w,0}^\Phi = x_{m,0}^\Phi/(1-x_{m,0}^\Phi)$ where $x_{m,0}^\Phi$ is the methane mole fraction in phase Φ at ($\mu_{w,0}$, $\mu_{m,0}$, $T_{f,0}$) and that $x_{m,0}^{\mathrm{L}} \sim 0$ for the liquid phase, Eqs. (1) and (2) lead to:

$$\frac{\Delta T_f}{T_{f,0}} = \frac{v_0^{\mathrm{H}}}{\Delta h_{f,0}}\left[(\gamma_{\mathrm{WL}} - \gamma_{\mathrm{WH}})\frac{2}{D_p} + \left(\frac{v_0^{\mathrm{L}}}{v_0^{\mathrm{H}}} - 1\right)(P^{\mathrm{L}} - P_0) + \frac{\Delta\mu_m}{v_0^{\mathrm{H}}}\frac{x_{m,0}^{\mathrm{H}}}{1-x_{m,0}^{\mathrm{H}}}\right] \quad [3]$$

where $\Delta h_{f,0} = \left(s_{f,0}^{\mathrm{L}} - s_{f,0}^{\mathrm{H}}\right)T_{f,0}$ is the bulk molar enthalpy of melting at ($T_{f,0}$, P_0). At this stage, it is often assumed that (1) the hydrate and liquid molar volumes are similar ($v_0^{\mathrm{H}} \sim v_0^{\mathrm{L}}$) and that (2) the methane chemical potential contribution is negligible ($\Delta\mu_m \sim 0$). With these approximations, one arrives at the Gibbs–Thomson equation which relates ΔT_f to D_p:

$$\frac{\Delta T_f}{T_{f,0}} = \frac{2v_0^{\mathrm{H}}(\gamma_{\mathrm{WL}} - \gamma_{\mathrm{WH}})}{\Delta h_{f,0}}\frac{1}{D_p} \quad [4]$$

Introducing Young's equation, $\gamma_{\mathrm{WL}} - \gamma_{\mathrm{WH}} = \gamma_{\mathrm{LH}}\cos\theta$ with $\theta = \pi$, Eq. (4) leads to the classical formulation: $\Delta T_f/T_{f,0} = -2\gamma_{\mathrm{LH}}v_0^{\mathrm{H}}/\Delta h_{f,0}D_p$. In contrast to this simplified equation, Eq. (3) is a revised version that accounts for the effect of methane gas in the free energy balance and the significant density difference between the liquid and hydrate.

In what follows, we determine the following parameters using independent molecular simulations to check the quantitative validity of Eq. (3): molar volumes v^{H} and v^{L}, molar enthalpy of melting $\Delta h_f = \left(h_w^{\mathrm{L}} + h_m^{\mathrm{V}}\right) - h_{m,w}^{\mathrm{H}}$ from the methane hydrate, liquid water, and methane vapor molar enthalpies. Fig. 3(b) shows v^{H}, v^{L}, h^{H}, and h^{L} at different bulk equilibrium conditions: (233 K, 1 atm), (262 K, 10 atm), and (286 K, 100 atm). We obtain $\Delta h_f = 8.35$ kJ·mol^{-1}, $v^{\mathrm{L}} = 1.85 \times 10^{-5}$ m^3·mol^{-1}, and $v^{\mathrm{H}} = 2.28 \times 10^{-5}$ m^3·mol^{-1} at $T = 286$ K and $P = 100$ atm. Such enthalpy of melting Δh_f leads to an entropy of melting $\Delta s_f = \Delta h_f/T_{f,0} = 29.3$ J·K^{-1}·mol^{-1} which is comparable to that reported in (42). In addition to these

parameters, the extended Gibbs–Thomson equation requires estimates for γ_{WH} and γ_{WL}. Here, we use the Irving-Kirkwood approach to determine γ_{WH} and γ_{WL} as described in SI *Text*. To increase statistical accuracy, especially for the hydrate phase, improved sampling was used by considering different microscopic configurations taken along the GCMC simulations. Fig. 3(b) shows γ_{WH} and γ_{WL} as a function of pore size. Each calculation was carried out at the temperature and pressure corresponding to the melting point upon confinement. To allow quantitative assessment of Eq. (3), γ^0_{WH} and γ^0_{WL} at the bulk melting point were also estimated as they are key quantities in the Gibbs–Thomson equation. As expected, γ_{WH} and γ_{WL} are constant around the asymptotic values γ^0_{WH} and γ^0_{WL} for large pores but deviate in the limit of very small pores. As shown in Fig. 3(b), such pore size dependence, which can be described using the concept of disjoining pressure (occurring as the two interfaces interact with each other for small pores), can be quantitatively described using the simple physical formula: $\gamma(D_p) = \gamma^0 + a\exp[-D_p/b]$ where a and b are the amplitude and range of the intermolecular forces responsible for the disjoining effect (43, 44). Using this approach, we found γ^0_{WL} = -117.8 J/m^2 and γ^0_{WH} = -52.4 J/m^2 (it was checked that the inferred interfacial tensions are only weakly dependent on the exact decay used for the disjoining contribution).

Fig. 3(c) compares the predictions from the classical and extended versions of the Gibbs–Thomson equation with the DCM results. For such a comparison, we consider the corrected pore size $D^*_p = D_p - 2\sigma^*$ where $\sigma^* \sim 0.33$ nm is the Lennard-Jones parameter for the wall/water interaction (we recall that D_p is defined as the distance between the carbon wall atoms so that it does not correspond to the pore size accessible to confined water/hydrate). This correction is needed as D^*_p is consistent with the volume accessible to the center of mass of the water and methane molecules (see density profiles discussed below). In particular, this definition ensures that the number of confined molecules goes to zero as $D^*_p \to 0$ (45). The classical version of the Gibbs–Thomson equation – which neglects the liquid/solid density difference and methane chemical potential – is found to qualitatively describe the linear scaling between the shift in melting point observed using molecular simulation and the reciprocal pore size (see comparison between the red circles and the gray shaded area). This result is consistent with previous experimental and molecular simulation results showing a qualitative scaling $\Delta T_f/T_{f,0} \sim 1/D_p$ (22–25, 27).

As for the extended Gibbs–Thomson equation, a few remarks are in order. First, by construction, because simulations were carried out along the bulk liquid-hydrate coexistence, the confined liquid and hydrate are in equilibrium at all T with a water/methane reservoir at the bulk coexistence pressure (i.e. $P^L = P^H = P^0$). This implies that the second term in Eq. (3) is equal to zero. As a result, by comparing the rest of this extended equation with the classical Gibbs–Thomson equation in Eq. (4) shows only one important difference: the methane chemical potential contribution. Fig. 3(c) shows that the Gibbs–Thomson equation using the interfacial tensions at the bulk melting point in combination with the chemical potential contribution as described in Eq. (3) correctly predicts the melting point depression observed using molecular simulation (comparison between red circles and the blue dashed line). This result shows that accounting for the methane contribution is important as it represents a non-negligible contribution to the expected Gibbs-Thomson shift in the hydrate melting point. As a last remark, even if the extended equation correctly predicts the melting point depression as a function of pore space D^*_p available to the fluid molecule center of mass, we note that the classical version of this equation leads to inferred pore sizes that do not strongly differ from the pore size D_p corresponding to the distance between opposite surfaces (from center of solid atoms on opposite walls). This result is important as it shows that the use of the classical Gibbs-Thomson equation to relate pore size and melting point shift remains reasonable – especially for large pores when the difference between D_p and D^*_p becomes negligible.

Free energy and phase stability. To probe the formation and dissociation kinetics of confined methane hydrate, we combined GCMC simulations with free energy calculations (details are provided in the Methods section). Using the umbrella-sampling technique, one can determine the free energy profile $\Omega(x)$ as a function of an order parameter x, which describes the transition from the liquid to the crystal phases [Fig. 4(a)]. The local order parameter $x = Q_6$ was used to identify methane hydrate ($Q_6 \sim 0.55$) and liquid water ($Q_6 \sim 0.35$). A perfect methane hydrate of dimensions $L_x = L_y = L_z \sim 2.36$ nm was prepared for bulk and confined methane hydrate in a slit pore of width $D_p \sim 2.86$ nm. Then, a harmonic potential $U^B(Q_6)$ is added to the energy calculated in the GCMC simulations to force the system to sample states corresponding to the given Q_6 value [This strategy is illustrated in Fig. 4(a) using the color squares]. Such a biased potential allows one to determine the probability distribution $P^B(Q_6)$ from the biased molecular simulations. Finally, the free energy profile is obtained by subtracting the biased potential energy from the biased probability distribution: $\Omega(Q_6) = -k_BT\ln[P^B(Q_6)] - U^B(Q_6)$.

Fig. 4(b) shows the free energy Ω/k_BT for the bulk (I) and confined (II, $D_p \sim 2.86$ nm) hydrate/liquid transitions as a function of the local order parameter Q_6 at different T. For the bulk transition [I in Fig. 4(b)], methane hydrate is found to be stable for $T < T_{f,0}$. For the confined transition [II in Fig. 4(b)], all free energy calculations are performed above the expected melting temperature T_f of confined methane hydrate as the umbrella sampling technique at lower T failed to converge (as discussed below, this is due to the slow formation/dissociation kinetics for methane hydrate). As expected, liquid water is the favorable phase at these T; indeed, free energy difference between methane hydrate and liquid water at these T is negative. To estimate the melting temperature of bulk and confined methane hydrate, the free energy difference $\Delta\Omega$ as a function of temperature T was extracted from the free energy profiles $\Omega(Q_6)$ shown in Fig. 4. A polynomial fit was performed to describe each free energy profile and estimate the location and free energy minimum corresponding to the liquid and hydrate phase. As shown in Fig. S9, we find that $\Delta\Omega$ depends linearly on T with the melting temperature corresponding to the temperature for which $\Delta\Omega \sim 0$. From such data, the bulk and confined melting temperatures, which are consistent with those found using the DCM, are $T_{f,0} = 302 \pm 16$ K and $T_f = 257 \pm 10$ K (the error bars are estimated from the uncertainty in extrapolating $\Delta\Omega \sim 0$).

To gain physical insights into the molecular mechanisms leading to methane hydrate formation/dissociation in confinement, we show in Fig. S10 the density profile of water ρ_w and methane ρ_m in the direction normal to the pore surface for

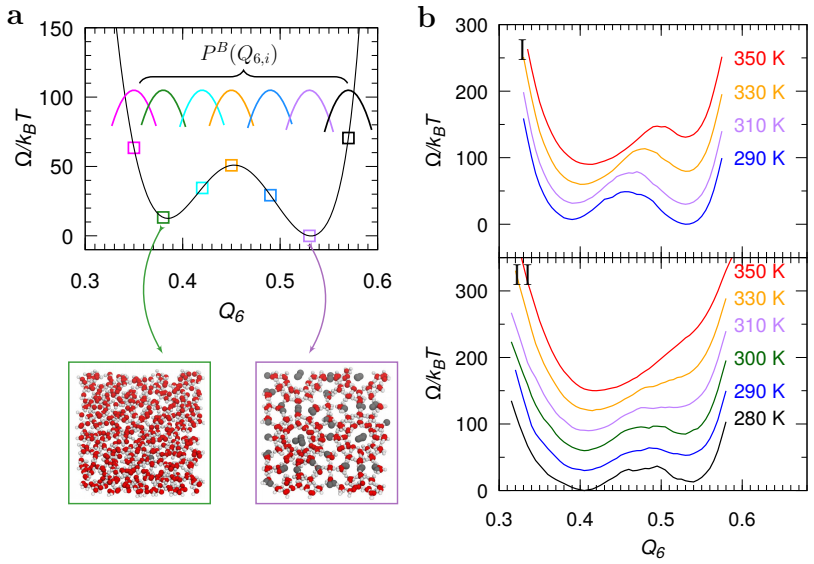

Fig. 4. Free energy calculations for methane hydrate and liquid water. (a) Umbrella sampling technique: the black solid line shows the free energy Ω as a function of the local order parameter Q_6. With this technique, a biased potential energy $U^B(Q_6)$ (see *text*) is used to force the system to explore configurations around a given Q_6 (as indicated by the color squares corresponding to different Q_6). Methane hydrate ($Q_6 \sim 0.53$) and liquid water ($Q_6 \sim 0.38$) correspond to the two minima observed in $\Omega(Q_6)$. The biased simulations provide estimates for the biased probability distribution $P^B(Q_6)$. The unbiased free energy $\Omega(Q_6)$ can be computed using the biased distribution minus the biasing potential energy: $\Omega(Q_6) = -k_BT \ln[P^B(Q_6)] - U^B(Q_6)$. The red and white spheres are the oxygen and hydrogen atoms of water while the gray spheres are the methane molecules. (b) Free energy profile $\Omega(Q_6)$ for bulk (I) and confined (II) methane hydrates at different T (as labelled in the graph). All free energies are normalized to k_BT.

several states taken along the free energy curve $\Omega(Q_6)/k_BT$: liquid water ($Q_{6,k}^{(0)} = 0.405$), transition state ($Q_{6,k}^{(0)} = 0.495$), a constrained state ($Q_{6,k}^{(0)} = 0.450$) between liquid water and transition state, and methane hydrate ($Q_{6,k}^{(0)} = 0.540$). As expected, in the liquid phase, water forms a film at the pore surface that is structurally ordered. Because of the increased positional and orientational ordering in this film, methane hydrate first appears at the surface of this film in the region at the interface between the surface region and the pore center. Such appearance occurs through the concomitant insertion of methane and structuring/ordering of water (the latter is supported by data corresponding to the $Q_6(z)$ profile). This localized methane hydrate then grows by extending towards the pore center and close to the pore surface. These results suggest that the strong ordering of water molecules close to the surface region promotes the formation of methane hydrate. In contrast, upon dissociation, the depletion in water molecules at the pore wall leads to a weaker hydrogen bonding interaction; the decrease of N_{HB} promotes the dissociation for confined methane hydrate. As discussed in the methods section, umbrella sampling calculations provide robust estimates for the free energy of different phases but the inferred transition path and underlying molecular mechanisms can depend on the selected order parameter. As a result, to verify the microscopic picture above, additional direct calculations were performed by monitoring the dissociation of a confined methane hydrate along a GCMC simulation carried out at a temperature above the confined melting point. Fig. S11 shows the water and methane density profiles and order parameter profile along the direction normal to the pore surface at different stages along dissociation. In agreement with the results discussed above, it is found that dissociation starts at a pore surface and then propagates towards the pore center.

For bulk methane hydrate, it has been shown that nucleation can proceed through direct crystallization from a solid nucleus or through transformation of an amorphous phase first appearing in the solution (46, 47). The observation of these two processes – either one step crystallization or two-step crystallization through the formation of an amorphous phase – was shown to depend on temperature with the two molecular mechanisms competing at moderate undercooling (32). For confined nucleation/dissociation, our microscopic data above – obtained independently using free energy calculations and simple Monte Carlo simulations – suggest that nucleation occurs through direct crystallization as the solid surface leads to significant surface ordering of water which, in turn, promotes hydrate cage formation. However, as described above, the fact that hydrate forms not in direct contact with the solid surface but in the region adjacent to the adsorbed water layer at the pore surface can be seen as parallel to the methane hydrate formation seen for bulk structures. Indeed, the adsorbed water layer coexisting with methane hydrate is playing a role somewhat equivalent to that of the amorphous phase observed under some specific thermodynamic conditions for bulk methane hydrate. In the next section, we develop a simple nucleation model in which crystallization is driven by the free energy balance between surface and volume contributions. Despite its simplicity, this model accounts for the disordered water layer at the pore surface since the interfacial tension between methane hydrate and the porous solid is calculated at coexistence conditions (which specifically include all atomistic/structural details of the confined phases).

Formation and dissociation kinetics. Despite its robustness, umbrella sampling fails to provide a rigorous estimate for the nucleation barrier $\Delta\Omega^*$ because the inferred value depends on the chosen order parameter and finite system size. To apprehend the nucleation process involved in the formation and dissociation of confined methane hydrate, we extend our investigation using a *mesoscale* description relying on thermodynamic ingredients identified in the molecular approach. In more detail, this coarse-grained strategy relies on the classical nucleation theory which describes nucleation at the mesoscopic level – therefore neglecting microscopic aspects including the role of molecular surface defects on crystallization/melting. Moreover, by relying on simple scalar parameters which are considered as homogeneous and constant, this approach fails to capture complex processes involving an irregular critical nucleus. Yet, as shown in the rest of this section, such a simple model is a robust framework to compare different methane hydrate nucleation mechanisms while relying on thermodynamic

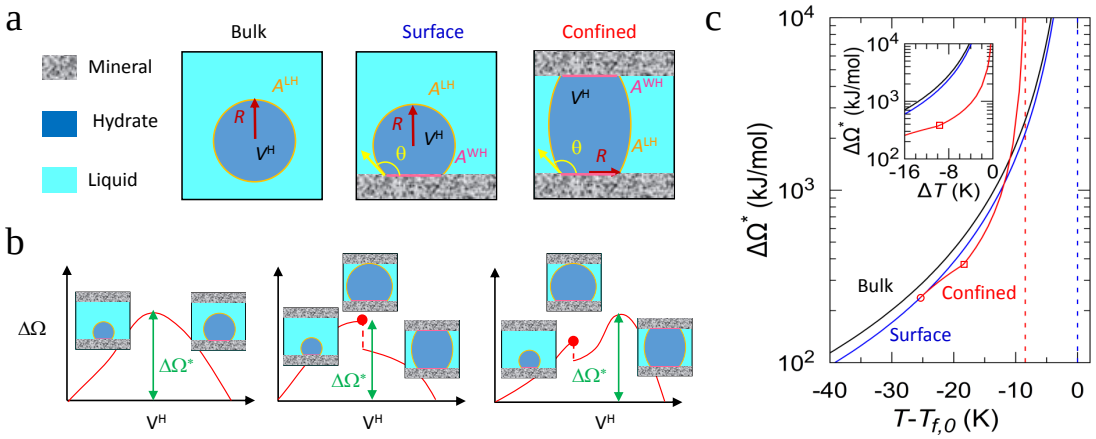

Fig. 5. Nucleation mechanisms for confined hydrate. (a) Schematic nucleus along bulk, surface, and confined nucleation mechanisms. Methane hydrate and liquid are shown as dark and light blue phases while the solid surface is shown in grey. V^{H} and R are the volume and radius of the nucleus while A^{LH} (orange line) and A^{WH} (pink line) are the hydrate/liquid and pore/hydrate interfaces. θ is the contact angle where the liquid, hydrate, and solid intersect. (**b**) Different schematic grand free energy along the confined nucleation mechanism. In all cases, the nucleation barrier $\Delta\Omega^*$ is shown by the green arrow. The red line shows the free energy change $\Delta\Omega$ as a function of the volume of the hydrate nucleus V^{H}. Starting from a hemispherical nucleus, three growth paths are possible. (center, right) The nucleus grows and transforms into a bridge nucleus as it reaches the opposite pore surface. Depending on the situation/parameters considered, the bridge grows with a free energy that is either lower or higher than the maximum free energy reached in the hemispherical nucleus configuration. (left) For large pores, the hemispherical nucleus reaches its stability limit before the hydrate nucleus reaches the opposite surface. In this case, the free energy barrier is given by the value reached at the instability point (this mechanism is strictly equivalent to surface nucleation). (c) Nucleation free energy barriers $\Delta\Omega^*$ calculated using the mesoscopic model for bulk (black), surface (blue) and confined (red) nucleation as a function of the temperature shift $T - T_{f,0}$ with respect to $T_{f,0}$. The blue and red dashed lines indicate the formation temperature for bulk (T_f) and confined ($T_{f,0}$) hydrate, respectively. The inset shows the same data $\Delta\Omega^*$ as a function of the temperature shift with respect to the formation temperature: $\Delta T = T - T_{f,0}$ for bulk/surface nucleation and $\Delta T = T - T_f(D_p)$ for confined nucleation. $D_p = 2.86$ nm is used for confined nucleation and all calculations are performed with $\gamma_{\mathrm{LH}} = 32$ mJ/m^2 as estimated in Ref. (54).

ingredients derived from our molecular simulation approach. As illustrated in Fig. 5(a), considering a porous medium coexisting with a bulk phase made up of gas methane and liquid water, three possible mechanisms must be considered: (1) bulk nucleation in the external liquid phase, (2) surface nucleation at the external surface of the porous solid, and (3) confined nucleation within the porous solid. Bulk nucleation corresponds to homogeneous nucleation through the formation of a spherical nucleus which grows until it becomes unstable. Both surface and confined nucleation correspond to heterogeneous mechanisms that initiate at the solid surface. Surface nucleation involves the formation of a surface hemispherical cap that grows until it becomes unstable at the critical nucleus size. Confined nucleation corresponds to the formation and growth of a surface hemispherical cap which transforms into a bridge as its height reaches the opposite pore surface [Fig. 5(b)]. Using the classical nucleation theory (48, 49), the exact nucleus shape for each mechanism is obtained by minimizing the surface energy at fixed methane hydrate volume V^{H} (50, 51). Regardless of the nucleus geometry, its grand free energy can be expressed as $\Omega = -P^{\mathrm{H}}V^{\mathrm{H}} - P^{\mathrm{L}}V^{\mathrm{L}} + \gamma_{\mathrm{WH}}A^{\mathrm{WH}} + \gamma_{\mathrm{WL}}A^{\mathrm{WL}} + \gamma_{\mathrm{LH}}A^{\mathrm{LH}}$. The excess grand free energy $\Delta\Omega = \Omega - \Omega^{\mathrm{L}}$ needed to generate such a nucleus with respect to the liquid phase ($\Omega^{\mathrm{L}} = -P^{\mathrm{L}}V + \gamma_{\mathrm{LW}}A$) writes:

$$\begin{aligned}\Delta\Omega &= (P^{\mathrm{L}} - P^{\mathrm{H}})V^{\mathrm{H}} + (\gamma_{\mathrm{WH}} - \gamma_{\mathrm{WL}})A^{\mathrm{WH}} + \gamma_{\mathrm{LH}}A^{\mathrm{LH}} \\ &= \Delta P V^{\mathrm{H}} - \gamma_{\mathrm{LH}}\cos\theta A^{\mathrm{WH}} + \gamma_{\mathrm{LH}}A^{\mathrm{LH}}\end{aligned} \quad [5]$$

where $V = V^{\mathrm{H}} + V^{\mathrm{L}}$ and $A = A^{\mathrm{WH}} + A^{\mathrm{WL}}$ are the total pore volume and surface. The second equality is obtained by using $\Delta P = P^{\mathrm{L}} - P^{\mathrm{H}}$ and Young equation $\gamma_{\mathrm{WL}} - \gamma_{\mathrm{WH}} = \gamma_{\mathrm{LH}}\cos\theta$. For each formation mechanism, the nucleation barrier $\Delta\Omega^*$ corresponding to the critical nucleus is given by the maximum free energy along the nucleation path $\Delta\Omega(V^{\mathrm{H}})$ (52).

Fig. 5(c) compares the free energy barriers for bulk, surface, and confined nucleation at a given shift $T - T_{f,0}$ with respect to the bulk formation temperature $T_{f,0}$ (all analytical calculations can be found in SI *text*). As expected, $\Delta\Omega^*$ diverges at $T_{f,0}$ for bulk and surface nucleation and at $T_f(D_p)$ for confined nucleation. The free energy barriers for the bulk and surface mechanisms are $\Delta\Omega^* = 4/3\pi\gamma_{\mathrm{LH}}R^{*2}$ and $\Delta\Omega^* = \gamma_{\mathrm{LH}}\pi R^{*2}(2 - 3\cos\theta + \cos^3\theta)/3$. As for confined nucleation, the exact critical nucleus and associated free energy barrier depend on $T - T_{f,0}$ as illustrated in Fig. 5(b). For small $T - T_{f,0}$ [red line, right of the red square in Fig. 5(c)], the critical nucleus corresponds to a hydrate bridge which forms as the hemispherical cap initiated at the pore surface becomes unstable. For intermediate $T - T_{f,0}$ [red line, between the red square and circle in Fig. 5(c)], $\Delta\Omega^*$ corresponds to a critical nucleus consisting of the hemispherical cap becoming unstable as it reaches the opposite pore surface. For large $T - T_{f,0}$ [red line, left of red circle in Fig. 5(c)], the critical nucleus consists of the hemispherical cap becoming unstable before reaching the opposite pore surface (as a result, in this temperature range, confined nucleation merges with surface nucleation). As shown in the inset Fig. 5(c), if we consider $\Delta\Omega^*$ at a given ΔT with respect to $T_{f,0}$ or $T_f(D_p)$, $\Delta\Omega^*$ is much lower for confined nucleation than for bulk and surface nucleation. This result suggests that the hydrate/liquid transition is much faster when confined in porous rocks, which is consistent with previous experimental data (28, 53). We also compare in Fig. S12(a) the critical nucleus size R^* for bulk, surface, and confined nucleation. As expected, $R^* = -2\gamma_{\mathrm{LH}}/\Delta P$ for bulk and surface nucleation are identical as can be inferred from the corresponding free energy approach described in SI *text*. On the other hand, for all $T - T_{f,0}$, R^* for confined nucleation is lower or equal to that for surface nucleation.

In line with the discussion above, when the critical nucleus consists of the hemispherical cap becoming unstable before reaching the opposite surface, R^* for confined nucleation is equal to its value predicted for surface nucleation. For bulk hydrate, in agreement with previous conclusion by Molinero and coworkers (31), the very large free energy barrier at moderate $T - T_{f,0}$ leads to non-physical long nucleation times τ. As noted in Ref. (31), this result suggests that the formation of bulk methane hydrate observed in real conditions never occurs through homogeneous nucleation. This interpretation is supported by our data which point to a smaller $\Delta\Omega^*$ for surface nucleation under the same conditions.

To provide a quantitative estimate of the formation/dissociation kinetics for confined hydrate, let us consider the experimental situation of a porous medium filled with liquid water and gas methane in equilibrium with a bulk reservoir. We assume that the system is brought to temperature T within a time insufficient to allow hydrate formation within the bulk phase (justified as typical experiments are performed on much shorter timescales than the characteristic nucleation time for bulk hydrate). With such conditions, both the confined and bulk phases are metastable when reaching $T < T_f(D_p)$. Using the nucleation theory, the nucleation rate $1/\tau = J \times A$ for surface and confined nucleation can be expressed as the surface area A developed by the porous material multiplied by the number of nuclei formed per unit of surface and unit of time, $J = \rho_s DZ \exp\left[-\Delta\Omega^*/k_BT\right]$ (ρ_s is the nucleus surface density, D_s the diffusivity, and Z the Zeldovich factor which accounts for the probability that a nucleus at the top of the free energy barrier does not melt and actually ends up forming hydrate). Assuming the same prefactor $\rho_s DZ$ for surface and confined nucleation, the latter expression allows comparing the nucleation times for these two mechanisms from the porous surface area A_p and external surface area A_e. For weak metastability [small $T_f(D_p) - T$], the confined nucleation time τ_c is much faster than at the external surface τ_s because $\Delta\Omega_c^* < \Delta\Omega_s^*$ and $A_p \gg A_e$. Similarly, for strong metastability [large $T_f(D_p) - T$], even if $\Delta\Omega_c^* = \Delta\Omega_s^*$, $\tau_c \ll \tau_s$ because $A_p \gg A_e$. These results are consistent with the work by Page and Sear (55) who investigated in-pore nucleation by means of Monte Carlo simulations for a 2D spin lattice. These authors reported evidence for a two-step nucleation process where a new thermodynamic phase first nucleates within the pore and then occurs in the bulk external phase. By considering the different mechanism rates, it was also shown that the effective nucleation rate is optimal for a well-defined pore size. Regardless of the exact confined nucleation mechanisms (hemispherical cap *versus* bridge), considering that A_p is proportional to the pore surface to volume ratio and, hence, to the reciprocal pore size, the nucleation time is expected to scale as $\tau_c \sim D_p$. In particular, the simple model proposed in our work predicts that the ratio between the nucleation times for confined and non-confined hydrate is proportional to the ratio of the external to pore specific surface area, $\tau_c/\tau_s \propto A_e/A_p$. Despite its simplicity, this semi-quantitative picture is consistent with experimental observations showing that confinement reduces the formation time from weeks to hours (20, 21). These calculations depend on the choice made for θ but our conclusions remain valid for all angles [Fig. 12(b) in SI].

Discussion

A molecular simulation approach is used to show that the thermodynamics of methane hydrate confined down to the nanoscale conforms the classical macroscopic picture as described by the Gibbs–Thomson equation. When confined in pores of a few molecular sizes, even if water and methane possess different wetting properties towards the host surface, they form a gas hydrate phase with structural properties very close to their bulk counterpart. A negative shift in the melting point is observed as a result of the pore/liquid interfacial tension being smaller than the pore/hydrate interfacial tension. Beyond thermodynamic aspects, by showing that confinement leads to facilitated methane hydrate formation and dissociation, our free energy calculations and mesoscopic nucleation model provide a theoretical support for the faster kinetics observed in experimental studies.

Together with the large body of experimental data available, the present results provide a unifying picture of methane hydrate in confined environments or in the vicinity of surfaces. While the description of confined methane hydrate adopted here is simplified compared to real systems, our findings remain meaningful to physical situations such as methane hydrate trapped in rocks on Earth or in other planets, comets, etc. They are also relevant to important energy and environmental aspects such as the expected impact of methane hydrate dissociation on global warming, the use of methane hydrate as energy storage devices, the formation of methane hydrate in pipelines, etc. Despite the simple approach used in this work, in addition to the melting point depression being consistent with available experimental data, the predicted methane hydrate formation and dissociation times provide a robust molecular scale picture of experiments in this field. In particular, considering the mechanisms and times associated with homogeneous and heterogeneous nucleation, methane hydrate is expected to form in the vicinity of pore surface and then to extend to the bulk external phase. In this context, beyond the temperature-dependent crossover between confined and surface nucleation, the predicted scaling between the induction time and pore size $\tau \sim D_p$ is an important result which sheds light on complex experimental behavior.

Despite these results, there is a number of aspects which were not considered explicitly in our approach. As shown by Borchardt and coworkers (21), even when very similar porous samples are considered, the detailed surface chemistry is expected to play a key role on the thermodynamics and kinetics of methane hydrate formation in confinement. In particular, while our approach only considered the formation (dissociation) of methane hydrate from (towards) liquid water, these authors observed using advanced structural characterization tools more complicated mechanisms involving the formation and distribution of hexagonal and/or disordered ice within the sample porosity. In this regard, pore sizes commensurate with the hydrate structure were selected so that we cannot rule out more complex mechanisms in case of important mismatch between pore space and crystal parameter. Moreover, while diffusion limitations of water and methane through the porosity is expected to affect the kinetics of methane hydrate formation and dissociation (56), they are not taken into account in our statistical mechanics approach which only considers thermodynamic aspects since mass transport and diffusion are not explicitly treated. However, in the classical nucleation

theory, such diffusion limitations only affect the prefactor and the typical nucleation time remains mostly driven – as a first order approximation – by the free energy metastability barrier. More importantly, despite the drawbacks identified above, the fact that our molecular simulation approach provides a picture consistent with experiments in almost every point makes our approach suitable to tackle issues related to methane hydrate in confined geometries.

Materials and Methods

Models. Methane is described as a Lennard-Jones (LJ) site with OPLS-UA force field parameters (57). Water is described using the TIP4P/Ice water model (58) which contains 4 sites: an LJ site on the oxygen, two point charges on the hydrogen atoms, and a site M corresponding to the O negative charge at a distance $d_{\rm OM} = 0.1577$ Å from the oxygen toward the hydrogen atoms along the H–O–H angle bisector. In this model, the O–H bond length is 0.9572 Å and the H–O–H angle 104.52°. As shown in Refs. (41, 59), TIP4P/Ice water combined with OPLS-UA methane accurately reproduces the experimental phase diagram of bulk methane hydrate. We use the stochastic procedure by Buch et al. (60) to generate a configuration with sI structure (27, 41, 60). The slit pores are built as follows. Each pore surface is of lateral dimensions $L_x = L_y \sim 2.38$ nm and made up of 11×11 squares whose vertices and centers are occupied by a solid atom. Solid atoms are maintained frozen in all simulations. The potential energy includes no intramolecular interactions as we consider a rigid water model, frozen solid, and united-atom methane model. The intermolecular potential between two atoms i and j includes a short-range repulsion and attractive dispersion described using the LJ potential: $u_{ij}^{LJ}(r) = 4\varepsilon_{ij}[(\sigma_{ij}/r)^{12} - (\sigma_{ij}/r)^{6}]$ where r is the distance separating i and j while ε_{ij} and σ_{ij} are the corresponding parameters. The LJ interactions are truncated beyond $r_c = 1.19$ nm. The like-atom parameters are given in Table S1 while the unlike-atom parameters are obtained using the Lorentz–Berthelot mixing rules. The intermolecular potential between i and j also includes the Coulomb contribution: $u_{ij}^{C}(r) = q_i q_j/(4\pi\varepsilon_0 r)$ where q_i and q_j denote the atomic charges (Table S1). Ewald summation is used to correct for the finite system size with an accuracy 10^{-5}. Considering the small box size used here, possible finite size effects cannot be ruled out. All calculations for bulk and confined hydrate were performed for the same lateral extension to minimize the impact of such potential effects. As will be shown below, we stress that the melting point extrapolated to an infinite pore matches accurately the bulk phase transition point as assessed using the direct coexistence method (DCM) and free energy calculations. Considering that finite size effects are expected to affect phase transitions for 2D and 3D systems to a different extent, this result suggests that our comparison between data for confined and bulk methane hydrate is relevant. Possible formation/dissociation hysteresis is another important technical limitation that should be discussed. First, we recall that both the DCM technique and free energy calculations are supposed to be free of such metastability issues. Indeed, by explicitly probing direct coexistence between two phases and/or by assessing accurately the free energy of each phase, these two methods allow overcoming the classical problems in molecular modeling applied to phase transitions (especially, crystallization). This is confirmed by the fact that these two methods lead to consistent results for both bulk and confined methane hydrate.

Molecular Dynamics and Monte Carlo simulations. Molecular Dynamics (MD) in the NPT ensemble is used to determine the molar volumes ($v^{\rm L}$, $v^{\rm H}$) and enthalpies ($h_w^{\rm L}$, $h_m^{\rm V}$, $h_{m,w}^{\rm H}$) at bulk coexistence conditions ($T_{f,0}$, P_0). The velocity-Verlet algorithm is used to integrate the equation of motion with an integration timestep of 1 fs. The temperature and pressure are controlled using Nosé-Hoover thermostat and barostat with a typical relaxation time of 2 ps for both NVT and NPT ensembles. All MD simulations were performed using *Lammps* (61). Monte Carlo simulations in the grand canonical ensemble (GCMC) are used in our DCM to determine the confined transition temperature T_f. In this ensemble, the system has a constant volume V, methane and water chemical potentials μ_m and μ_w, and temperature T. Monte Carlo moves in the grand canonical ensemble include molecule rotations, translations, insertions and deletions for both water and methane. A move from an old (o) to a new (n) microscopic states is accepted or rejected using a Metropolis scheme with an acceptance probability $P_{acc} = \min\{1, p^n_{\mu_m\mu_w VT}/p^o_{\mu_m\mu_w VT}\}$ where $p_{\mu_m\mu_w VT}$ corresponds to the density of states in the grand canonical ensemble:

$$p_{\mu_m\mu_w VT}(\mathbf{s}^N) \propto \frac{V^N}{\Lambda_m^{3N_m}\Lambda_w^{3N_w} N_m! N_w!} \prod_{i=m,w} \exp\left(\frac{N_i\mu_i}{k_BT}\right) \exp\left(\frac{-U(\mathbf{s}^N)}{k_BT}\right) \quad [6]$$

with $\Lambda_i = h/\sqrt{2\pi m_i k_B T}$ the thermal wavelength for molecule i (m, w). N_w and N_m are the numbers of water and methane molecules, $\mathbf{s}^N$ is the coordinate set of the $N = N_w + N_m$ molecules in a microscopic configuration whose intermolecular energy is $U(\mathbf{s}^N)$.

Starting from initial molecular configurations, isobaric-isothermal ensemble molecular dynamics is performed for at least 6 ns to ensure equilibration is reached. Thermodynamic properties are then averaged using configurations taken in the last 2 ns to estimate the molar volume and enthalpy for methane hydrate, liquid water and methane vapor. As for the GCMC simulations, energy, number of methane and water molecules are averaged over configurations taken every 50000 Monte Carlo moves (where one move consists of a molecule translation, rotation, insertion or deletion). Each GCMC simulation consists of at least 10^{10} moves (corresponding to at least 10^6 moves per water/methane molecule). Translation, rotation, insertion and deletion are attempted with the following probabilities: 40%, 40%, 10% and 10%. With such numbers, the typical Monte Carlo acceptance probability in the Metropolis scheme is about 35% for translation/rotation and 0.2% for insertion/deletion. While the latter number is rather low, the very large number of Monte Carlo moves considered provide efficient sampling and equilibration (as evidenced by the fact that the DCM calculations lead to results consistent with those obtained using free energy calculations).

Free energy calculations. Umbrella sampling is used to determine the free energy Ω as a function of the local order parameter Q_6. This quantity, which allows identifying liquid water and methane hydrate (62), is determined for a given oxygen O_i as:

$$Q_{6,i} = \left(\frac{4\pi}{13}\sum_{m=-6}^{6} \mid \mathbf{Q}_{6m,i} \mid^2\right)^{1/2} \quad [7]$$

where $\mathbf{Q}_{6m,i}$ are complex vectors defined as $Q_{6m,i} = 1/N_{b,i}\sum \mathbf{Y}_{6m}(\mathbf{r}_{ij})$. The summation over $j = 1$ to $N_{b,i}$ runs for all neighbor oxygen within a distance $r_c' = 0.35$ nm) while $\mathbf{Y}_{6m}(\mathbf{r}_{ij})$ are the spherical harmonics that depend on the vector $\mathbf{r}_{ij} = \mathbf{r}_j - \mathbf{r}_i$.

The free energy was determined using umbrella sampling with biased grand canonical Monte Carlo simulations. Starting from methane hydrate, we force its transformation into liquid water using a Q_6 dependent biasing potential $U^B(Q_6)$. Such biased simulations yield the biased probability distribution $P^B(Q_6)$ which can be corrected from the biased potential energy to determine the free energy as described in the main text. To sample the entire domain Q (0.3 – 0.6), we consider $N_s = 61$ windows with a spacing of 0.05 so that N_s biased Monte Carlo simulations are carried out with the corresponding $Q_{6,k}^0$. In more detail, for the k-th window, the following biasing harmonic potential is used: $U_k^B(Q_6) = 1/2K[Q_6 - Q_{6,k}^0]^2$ where $K = 5 \times 10^7$ K is the force constant and $Q_{6,k}^0$ the central value. We use the weighted average of the unbiased probability distribution of each window $P_k^U(Q_6)$ to determine the full-unbiased probability distribution $P^U(Q_6)$:

$$P^U(Q_6) = \sum_{k=1}^{N_s} N_k P_k^U(Q_6) \exp\left(-\frac{U_k^B(Q_6) - \Omega_k(Q_6)}{k_BT}\right) \quad [8]$$

where $P_k^U(Q_6)$ and N_i are the unbiased probability distribution and the number of samples, respectively, in the k-th window. $\Omega_k(Q_6)$ is

the metastability free energy which can be calculated according to:

$$\exp\left(-\frac{\Omega_k(Q_6)}{k_BT}\right) = \int dQ_6 P^U(Q_6) \exp\left(-\frac{U_k^B(Q_6)}{k_BT}\right) \quad [9]$$

Starting from Eq. (8) with $\Omega_k(Q_6) = 0$, we iterate self-consistently between Eqs. (9) and (8) until convergence is reached.

While umbrella sampling probes unambiguously the free energy of different phases, they can be prone to biases related to the choice made for the order parameter when estimating free energy barriers. On the one hand, the free energy minima found for each involved phase is independent of the chosen order parameter – therefore leading to an ambiguous definition for the phase transition temperature/pressure. This result is confirmed by the fact that out free energy calculations lead to the same formation/dissociation temperature as that inferred from the direct coexistence method. On the other hand, the estimated free energy barrier and detailed molecular mechanisms involved might depend on the specific transition path followed by the system (which is driven by the order parameter used to conduct the umbrella sampling).

ACKNOWLEDGMENTS. D. Jin acknowledges financial support from China Scholarship Council (CSC 201506450015). We thank F. Calvo, J. L. Barrat, C. Picard, L. Scalfi, and B. Rotenberg, L. Borchardt and S. Gratz, for interesting discussions.

References

1. E.D. Sloan, Fundamental Principles and Applications of Natural Gas Hydrates. *Nature* **426**, 353–363 (2003).
2. C.A. Koh, A.K. Sum, E.D. Sloan, State of the art: Natural gas hydrates as a natural resource. *J. Nat. Gas Sci. Eng.* **8**, 132–138 (2012).
3. E.D. Sloan, C.A. Koh, *Clathrate Hydrates of Natural Gases*, 3rd edn (CRC Press, 2007).
4. G.J. MacDonald, The Future of Methane as an Energy Resource. *Annu. Rev. Energy* **15**, 53–83 (1990).
5. P. Serov *et al.*, Postglacial response of Arctic Ocean gas hydrates to climatic amelioration. *Proc. Natl. Acad. Sci. U.S.A* **114**, 6215–6220 (2017).
6. B.J. Phrampus, M.J. Hornbach, Recent Changes to the Gulf Stream Causing Widespread Gas Hydrate Destabilization. *Nature* **490**, 527–530 (2012).
7. W.T. Wood *et al.*, Decreased Stability of Methane Hydrates in Marine Sediments Owing to Phase-boundary Roughness. *Nature* **420**, 656–660 (2002).
8. V. Formisano *et al.*, Detection of Methane in the Atmosphere of Mars. *Science* **54**, 1758–1761 (2004).
9. H. Lee *et al.*, Tuning clathrate hydrates for hydrogen storage. *Nature* **434**, 743–746 (2005).
10. A. Patt *et al.*, A grand canonical Monte Carlo study of the N_2, CO, and mixed N_2–CO clathrate hydrates. *J. Phys. Chem. C* **122**, 18432–18444 (2018).
11. C. Petuya *et al.*, Selective trapping of CO_2 gas and cage occupancy in CO_2–N_2 and CO_2–CO mixed gas hydrates. *Chem. Commun.* **54**, 4290–4293 (2018).
12. N.J. English, J.S. Tse, Mechanisms for thermal conduction in methane hydrate. *Phys. Rev. Lett.* **103**, 015901–015905 (2009).
13. J.W. Pohlman, J.S. Tse, Enhanced CO_2 uptake at a shallow Arctic Ocean seep field overwhelms the positive warming potential of emitted methane. *Proc. Natl. Acad. Sci. U.S.A* **114**, 5355–5360 (2017).
14. K.W. Hall, S. Carpendale, P.G. Kusalik, Evidence from mixted hydrate nucleation for a funnel model of crystallization. *Proc. Natl. Acad. Sci. U.S.A* **113**, 12041–12046 (2016).
15. Z. Duan *et al.*, The influence of temperature, pressure, salinity and capillary force on the formation of methane hydrate. *Geosci. Frontiers* **2**, 125–135 (2011).
16. M.E. Casco *et al.* Methane hydrate formation in confined nanospace can surpass nature. *Nat. Commun.* **6**, 6432–6440 (2015).
17. F. Wang *et al.*, Direction Controlled Methane Hydrate Growth. *Cryst. Growth Des.* **15**, 5112–5117 (2016).
18. J. Ghosh *et al.*, Clathrate hydrates in interstellar environment. *Proc. Natl. Acad. Sci. U.S.A* **116**, 1526–1531 (2019).
19. L. Borchardt *et al.*, Illuminating solid gas storage in confined spaces - methane hydrate formation in porous model carbons. *Phys. Chem. Chem. Phys.* **18**, 20607–20614 (2016).
20. L. Borchardt, M.E. Casco, J. Silvestre-Albero, Methane Hydrate in Confined Spaces: An Alternative Storage System. *Chem. Phys. Chem.* **19**, 1298–1314 (2018).
21. M.E. Casco *et al.*, Experimental evidence of confined methane hydrate in hydrophilic and hydrophobic model carbons. *J. Phys. Chem. C* **123**, 24071–24079 (2019).
22. Y. Seo, H. Lee, T. Uchida, Methane and Carbon Dioxide Hydrate Phase Behavior in Small Porous Silica Gels: Three-Phase Equilibrium Determination and Thermodynamic Modeling. *Langmuir* **18**, 9164–9170 (2002).
23. T. Uchida *et al.*, Effects of Pore Sizes on Dissociation Temperatures and Pressures of Methane, Carbon Dioxide, and Propane Hydrates in Porous Media. *J. Phys. Chem. B* **106**, 820–826 (2002).
24. K. Seshadri, J.W. Wilder, D.H. Smith, Measurements of Equilibrium Pressures and Temperatures for Propane Hydrate in Silica Gels with Different Pore-Size Distributions. *J. Phys. Chem. B* **105**, 2627–2631 (2001).
25. R. Anderson *et al.*, Experimental Measurement of Methane and Carbon Dioxide Clathrate Hydrate Equilibria in Mesoporous Silica. *J. Phys. Chem. B* **107**, 3507–3514 (2003).
26. I. Deroche, T. Jean Daou, C. Picard, B. Coasne, Reminiscent capillarity in subnanopores. *Nat. Commun.* **10**, 4642 (2019).
27. S.N. Chakraborty, L.D. Gelb, A Monte Carlo Simulation Study of Methane Clathrate Hydrates Confined in Slit-Shaped Pores. *J. Phys. Chem. B* **116**, 2183–2197 (2012).
28. P. Linga *et al.*, Enhanced rate of gas hydrate formation in a fixed bed column filled with sand compared to a stirred vessel. *Chem. Eng. Sci.* **68**, 617–623 (2012).
29. M.R. Walsh *et al.*, Microsecond simulations of spontaneous methane hydrate nucleation and growth. *Science* **326**, 1095–1098 (2009).
30. D. Yuhara *et al.*, Nucleation rate analysis of methane hydrate from molecular dynamics simulations. *Faraday Discuss.* **179**, 463–474 (2015).
31. B.C. Knott *et al.* Homogeneous Nucleation of Methane Hydrates: Unrealistic under Realistic Conditions. *J. Am. Chem. Soc.* **134**, 19544–19547 (2012).
32. Arjun, T.A. Berendsen, P.G. Bolhuis, Unbiased atomistic insight in the competing nucleation mechanisms of methane hydrates. *Proc. Natl. Acad. Sci. U.S.A* **116**, 19305–19310 (2019).
33. R. Liang *et al.*, Nucleation and dissociation of methane clathrate embryo at the gas-water interface. *Proc. Natl. Acad. Sci. U.S.A* **116**, 23410–23415 (2019).
34. S.P. Kang, Y. Seo, W. Jang, Kinetics of Methane and Carbon Dioxide Hydrate Formation in Silica Gel Pores. *Energy Fuels* **23**, 3711–3715 (2009).
35. D. Bai *et al.*, Microsecond Molecular Dynamics Simulations of the Kinetic Pathways of Gas Hydrate Formation from Solid Surfaces. *Langmuir* **27**, 5961–5967 (2011).
36. K. Yan *et al.*, Molecular Dynamics Simulation of the Crystal Nucleation and Growth Behavior of Methane Hydrate in the Presence of the Surface and Nanopores of Porous Sediment. *Langmuir* **32**, 7975–7984 (2016).
37. S. Liang, D. Rozmanov, P.G. Kusalik, Crystal growth simulations of methane hydrates in the presence of silica surfaces. *Phys. Chem. Chem. Phys.* **13**, 19856–19864 (2011).
38. S.A. Bagherzadeh *et al.*, Influence of Hydrated Silica Surfaces on Interfacial Water in the Presence of Clathrate Hydrate Forming Gases. *J. Phys. Chem. C* **116**, 24907–24915 (2012).
39. B. Coasne, S.K. Jain, L. Naamar, K.E. Gubbins, Freezing of argon in ordered and disordered porous carbon. *Phys. Rev. B* **76**, 085416–085415 (2007).
40. B. Coasne, J. Czwartos, M. Sliwinska-Bartkowiak, K.E. Gubbins, Effect of Pressure on the Freezing of Pure Fluids and Mixtures Confined in Nanopores. *J. Phys. Chem. B* **113**, 13874–13881 (2009).
41. D. Jin, B. Coasne, Molecular Simulation of the Phase Diagram of Methane Hydrate: Free Energy Calculations, Direct Coexistence Method, and Hyperparallel Tempering. *Langmuir* **33**, 11217–11230 (2017).
42. L.C. Jacobson, V. Molinero, Can Amorphous Nuclei Grow Crystalline Clathrates? The Size and Crystallinity of Critical Clathrate Nuclei. *J. Am. Chem. Soc.* **133**, 6458–6463 (2011).
43. F. Celestini, A. ten Bosch, Importance of interfacial coupling on the formation and growth of metastable phases. *Phys. Rev. E* **50**, 1836–1842 (1994).
44. R.J.-M. Pellenq, B. Coasne, R.O. Denoyel, O. Coussy, Simple Phenomenological Model for Phase Transitions in Confined Geometry. 2. Capillary Condensation/Evaporation in Cylindrical Mesopores. *Langmuir* **25**, 1393–1402 (2009).
45. B. Coasne, P. Ugliengo, Atomistic Model of Micelle-Templated Mesoporous Silicas: Structural, Morphological, and Adsorption Properties. *Langmuir* **28**, 11131–11141 (2012).
46. L.C. Jacobson, W. Hujo, V. Molinero, Amorphous Precursors in the Nucleation of Clathrate Hydrates. *J. Am. Chem. Soc.* **132**, 11806–11811 (2010).
47. A. Arjun, P.G. Bolhuis, Molecular Understanding of Homogeneous Nucleation of CO_2 Hydrates Using Transition Path Sampling. *J. Phys. Chem. B* **125**, 338–349 (2021).
48. S. Auer, D. Frenkel, Quantitative Prediction of Crystal-Nucleation Rates for Spherical Colloids: A Computational Approach. *Annu. Rev. Phys. Chem.* **55**, 333–361 (2004).
49. Z.M. Aman, C.A. Koh, Interfacial phenomena in gas hydrate systems. *Chem. Soc. Rev.* **45**, 1678–1690 (2016).
50. F. Restagno, L. Bocquet, T. Biben, Metastability and Nucleation in Capillary Condensation. *Phys. Rev. Lett.* **84**, 2433–2436 (2000).
51. B. Lefevre *et al.*, Intrusion and extrusion of water in hydrophobic mesopores. *J. Chem. Phys.* **120**, 4927–4938 (2004).
52. Y.E. Altabet, A. Haji-Akbari, P. G. Debenedetti, Effect of material flexibility on the thermodynamics and kinetics of hydrophobically induced evaporation of water. *J. Chem. Phys.* **114**, 2548–2555 (2017).
53. A. Phan, D.R. Cole, A. Striolo, Aqueous Methane in Slit-Shaped Silica Nanopores: High Solubility and Traces of Hydrates. *J. Phys. Chem. C* **118**, 4860–4868 (2014).
54. S. Mirzaeifard, P. Servio, A.D. Rey, Multiscale Modeling and Simulation of Water and Methane Hydrate Crystal Interface. *Cryst. Growth Des.* **19**, 5142–5151 (2019).
55. A. J. Page, R. P. Sear, Heterogeneous Nucleation in and out of Pores. *Phys. Rev. Lett.* **97**, 065701–065705 (2006).
56. J. Zhao *et al.*, Growth Kinetics and Gas Diffusion in Formation of Gas Hydrates from Ice. *J. Phys. Chem. C* **124**, 12999–13007 (2020).
57. W.L. Jorgensen, D.S. Maxwell, J. Tirado-Rives, Development and Testing of the OPLS All-Atom Force Field on Conformational Energetics and Properties of Organic Liquids. *J. Am. Chem. Soc.* **118**, 11225–11236 (1996).
58. J.L.F. Abascal *et al.*, A Potential Model for the Study of Ices and Amorphous Water: TIP4P/ICE. *J. Chem. Phys.* **122**, 234511 (2005).
59. M.M. Conde, C. Vega, Determining the Three-phase Coexistence Line in Methane Hydrates Using Computer Dimulations. *J. Chem. Phys.* **133**, 064507 (2010).
60. V. Buch, P. Sandler, J. Sadlej, Simulations of H_2O Solid, Liquid, and Clusters, with an Emphasis on Ferroelectric Ordering Transition in Hexagonal Ice. *J. Phys. Chem.* **102**, 8641–8653 (1998).
61. S. Plimpton, Fast Parallel Algorithms for Short-Range Molecular Dynamics. *J. Comput. Phys.* **117**, 1–19 (1995).
62. R. Radhakrishnan, B.L. Trout, A New Approach for Studying Nucleation Phenomena Using Molecular Simulations: Application to CO_2 Hydrate Clathrates. *J. Chem. Phys.* **117**, 1786 (2002).